A Constant Switching Frequency Finite-Control-Set Predictive Current Control Scheme of a Five-Phase Inverter With Duty-Ratio Optimization

Cheng Xue, Wensheng Song, *Member, IEEE*, Xuesong Wu, and Xiaoyun Feng

***Abstract*—As is well known, the additional low-order harmonic currents and the huge computation amount of the cost function value with all available control sets are the two special issues of finite-control-set model predictive current control (FCS-MPCC) for multiphase inverters. Thus, this paper proposes a FCS-MPCC scheme with duty-ratio optimization for five-phase inverters. First, a group of the reconstructed virtual voltage vectors (V^3) with low-order harmonic elimination is defined and employed as the control sets in FCS-MPCC scheme. Thus, it leads to no requirement for harmonic items and weighting factors existing in the cost function. Then, a combination of zero vectors and the selected V^3 during each control horizon is adopted to rearrange the pulse sequence, which can realize constant switching frequency. In addition, the durations of the selected V^3 and zero vectors during each control horizon are also estimated to minimize the steady-state current ripples in different subspaces based on the cost function optimization. Finally, a comparison of the proposed V^3-FCS-MPCC scheme and the other FCS-MPCCs are presented in simulation and experimental test. Simulation and experimental results verify that the proposed V^3-FCS-MPCC scheme can remain the simplified structure, fast dynamic performance, constant switching frequency, and achieve minimum current ripples in different subspaces.**

***Index Terms*—Constant switching frequency, current control, duty ratio, finite control set (FCS), model predictive control (MPC), multiphase inverters, virtual voltage vector (V^3).**

I. Introduction

THE interest in the area of multiphase inverters has substantially increased during the last decade because of the potential advantages that they offer for multiphase machine drives [1]–[4]. Compared with the conventional three-phase power converter system, multiphase inverters have several salient features: First, higher power and current can be delivered using power electronic devices in huge-power and low-voltage occasion, such as: electromagnetic launch system, railway locomotive traction drive, marine and aerospace propulsion. Second, there are more control variables that can be manipulated to afford stronger fault tolerance [5]–[8], and the enhanced reliability is subsequently coming. Third, multiphase inverters can also provide an improved magnetomotive force waveform, lower torque pulsation [9], [10], and higher torque density for their applications [11], [12].

Model predictive control (MPC) has been becoming a hot topic of academic and industry for more than three decades, and the most classical form is the finite-control-set MPC (FCS-MPC) [13]. Among various kinds of FCS-MPC methods, model predictive current control with the finite-control-set (FCS-MPCC) is one of the most important and classical solutions in power electronics. MPC schemes have been widely reported for three-phase inverter applications [14] and popularized to a five-phase inverter driving a star-connected *R–L* load [15], [16]. FCS-MPCC is a typical direct-current control scheme that predicts the future evolution of currents in discrete time using a predictive model. It takes into account the discrete nature of power converters to solve the online optimization problem using a single cost function and does not require an external modulator [17]. The switching vector that minimizes cost function is selected as the output of the controller. The FCS-MPCC scheme has an intuitive concept and straightforward implementation. Furthermore, the considered variables and control objectives of the system can be easily presented by designing a specific cost function with adjustable weighting factors. However, FCS-MPCC needs to solve the optimization problem during each control horizon, which leads to the heavy calculation amount. Especially, for long steps prediction and multilevel or irregular converter topologies application, the calculation complexity can rise exponentially [17]. As presented in [18] and [19], a synchronous current control scheme with a full set of switching states taken as the input control set of the FCS-MPCC for a five-phase drive system was addressed. Usually, a heavy calculation amount means that a lower sampling frequency should be employed for the sake of executing solution procedure, which will increase current ripple and deteriorate current waveform quality.

In order to reduce the calculation effort due to the increased number of iterations, various advanced techniques have been applied for a multiphase system. A simplified algorithm that employs adjacent voltage vector was proposed to reduce the available voltage vectors of the control set in [20]. Similarly, Lim *et al.* [21] proposed a computation reduction solution that eliminates unfeasible switching states inherent in reduced-switch-

Manuscript received January 2, 2017; revised March 26, 2017; accepted May 6, 2017. Date of publication May 23, 2017; date of current version January 3, 2018. This work was supported in part by the National Natural Science Foundation of China under Project 51577160. Recommended for publication by Associate Editor J. Rodriguez. *(Corresponding author: Wensheng Song.)*

The authors are with the School of Electrical Engineering, Southwest Jiaotong University, Chengdu 610031, China (e-mail: chengx_swjtu@163.com; songwengsheng@163.com; wxs@my.swjtu.edu.cn; fengxy@swjtu.edu.cn).

Color versions of one or more of the figures in this paper are available online at http://ieeexplore.ieee.org.

Digital Object Identifier 10.1109/TPEL.2017.2707440

count inverters. These two methods can reduce computational burden effectively but at the expense of worse control optimality. Additionally, according to predefined constraints, a predictive control technique was adopted in [22] to reduce the available switching states of voltage-source inverters. However, the shortcoming of the adopted scheme is the weak algorithm portability. Therefore, how to reduce the computational cost in FCS-MPCC scheme for a multiphase drive system still needs to be studied further.

Recently, to achieve excellent steady-state performance of three-phase inverter-fed motor drive systems, duty-cycle control concept was proposed to be applied in FCS-MPC [23], [24]. For example, in order to reduce torque ripple of an induction motor, a combination of the selected active voltage vector and null vector in each control horizon is adopted in the proposed FCS-MPC reported in [23]. Different from traditional optimal duty-cycle control, Zhang and Yang [23] reported that the way of selecting voltage vector first based on the principle of cost function minimization can no longer remain optimal in minimizing torque and flux errors. Thus, it realizes vector selection and duty-ratio optimization simultaneously. The duration of the active vector is obtained from a deadbeat torque controller. Consequently, better torque performance under lower sampling frequency condition can be observed. In addition, better steady-state performance during wide speed range can be achieved, compared with the traditional duty-cycle optimal control schemes. As for a multiphase drive system, the work with an evaluation of the FCS-MPC quality using duty-ratio optimization is only discussed in [25], where a five-phase inverter is considered for a two-motor three-phase drive. However, the work reported in [25] is not available for an independent multiphase load system.

This paper aims to deal with the aforementioned issues in the FCS-MPCC for five-phase drive systems. Virtual voltage vectors (V^3s) are reconstructed first for releasing the computational burden of digital signal processor. Then, a new integrated FCS-MPCC method with the duty-ratio estimation of V^3s in five-phase inverters is proposed, which can enhance torque waveform quality, reduce the low-order harmonic components of phase currents, and keep constant switching frequency for the power switches. Compared with the existing FCS-MPCC schemes for multiphase inverters, the salient features of the proposed FCS-MPCC scheme can be summarized as follows.

1) Proposing an integrated FCS-MPCC method with duty-ratio optimization and making it expandable to five-phase inverters even other multiphase system.
2) Employing the predefined V^3s as the control set to reduce the low-order current harmonics. Hence, it is not necessary to design harmonic item and the weighting factor in the cost function.
3) Enhancing the output current quality, comparing with the several traditional FCS-MPCC schemes. Steady-state performance will be better, while the fast dynamic response is reserved.
4) Taking the discrete nature of power converters into account and selects the best V^3 by minimizing a predefined cost function. Hence, the simplified structure is reserved and no modulation stage is required.

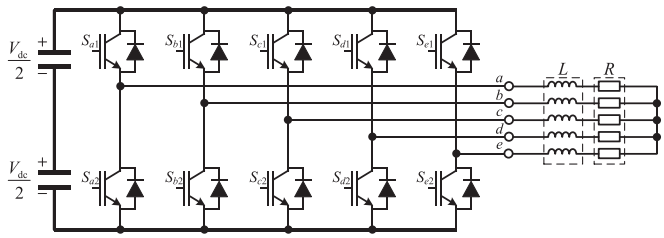

Fig. 1. Five-phase voltage-source inverter power circuit.

5) Realizing constant switching frequency for inverters.

This paper is organized as follows. The discrete model of a five-phase inverter system is described and the basic concept of the FCS-MPCC algorithm is presented in Section II. Section III explains the proposed scheme with duty-ratio optimization. Section IV shows the comparative experimental results of the proposed method and traditional FCS-MPCC schemes. Finally, Section V concludes this paper.

II. System Modeling and Traditional FCS-MPCC of Five-Phase Inverters

The main topology of a two-level five-phase voltage-source inverter connected to a passive *R--L* load is depicted in Fig. 1. The load is taken star connected and the input dc-link voltage $V_{\rm dc}$ is regarded as being constant. Five-phase bridge legs are symboled and expressed as *a*, *b*, *c*, *d*, *e*, respectively. Symbol *S* with subscript represents the drive signal of each switch device. The upper and lower devices of each leg operate in a complementary manner.

A. Voltage Vectors Distribution

The five-phase inverter has 32 voltage vectors, which can be defined as the binary value of $V_i = S_{a1}S_{b1}S_{c1}S_{d1}S_{e1}$. "1" indicates the upper switch of the corresponding leg is on, while "0" indicates the lower switch is on. Since five-phase variables present four degrees of freedom with the exception of zero-sequence components, two space vectors should be used in order to define the equivalent transformation of five-phase variables [26]. The fundamental components of the inverter variables and the harmonics with order $k = 10m \pm 1$ ($m = 1, 2, 3\ldots$) are transformed into the α-β subspace, whereas the harmonics with $k = 10m \pm 3$ ($m = 1, 2, 3\ldots$) are mapped into the *x*-*y* subspace. The voltage vectors can be expressed with the switching functions as

$$\begin{aligned}\boldsymbol{V}_{\alpha\beta} &= V_\alpha + jV_\beta \\ &= \frac{2}{5}V_{dc}(S_{a1} + \chi S_{b1} + \chi^2 S_{c1} + \chi^3 S_{d1} + \chi^4 S_{e1}) \quad (1)\\ \boldsymbol{V}_{\rm xy} &= V_x + jV_y \\ &= \frac{2}{5}V_{dc}(S_{a1} + \chi S_{c1} + \chi^2 S_{e1} + \chi^3 S_{b1} + \chi^4 S_{d1}) \quad (2)\end{aligned}$$

where $\chi = \exp(j2\pi/5)$.

The α-β and *x*-*y* subspace voltage vectors can be described in Fig. 2(a) and (b), respectively. According to the amplitude, the voltage vectors in α-β subspace are classified into four types:

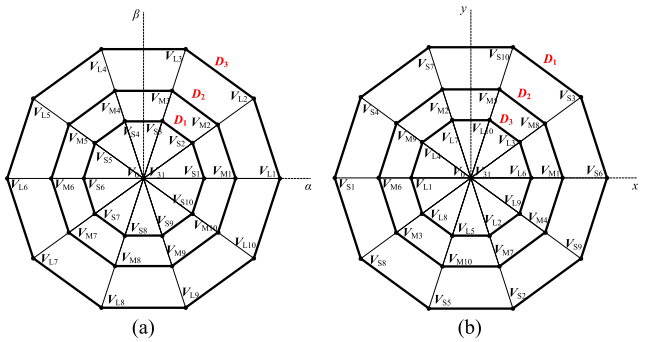

Fig. 2. Space vector diagram of five-phase inverters in two subspaces. (a) α-β subspace. (b) x-y subspace.

TABLE I
SPACE VECTOR GROUPS AND CORRESPONDING SWITCHING STATES

Group	Switching States
Large	$\boldsymbol{V}_{\mathrm{L}1}(11001), \boldsymbol{V}_{\mathrm{L}2}(11000), \boldsymbol{V}_{\mathrm{L}3}(11100), \boldsymbol{V}_{\mathrm{L}4}(01100), \boldsymbol{V}_{\mathrm{L}5}(01110), \boldsymbol{V}_{\mathrm{L}6}(00110), \boldsymbol{V}_{\mathrm{L}7}(00111), \boldsymbol{V}_{\mathrm{L}8}(00011), \boldsymbol{V}_{\mathrm{L}9}(10011), \boldsymbol{V}_{\mathrm{L}10}(10001)$
Medium	$\boldsymbol{V}_{\mathrm{M}1}(10000), \boldsymbol{V}_{\mathrm{M}2}(11101), \boldsymbol{V}_{\mathrm{M}3}(01000), \boldsymbol{V}_{\mathrm{M}4}(11110), \boldsymbol{V}_{\mathrm{M}5}(00100), \boldsymbol{V}_{\mathrm{M}6}(01111), \boldsymbol{V}_{\mathrm{M}7}(00010), \boldsymbol{V}_{\mathrm{M}8}(10111), \boldsymbol{V}_{\mathrm{M}9}(00001), \boldsymbol{V}_{\mathrm{M}10}(11011)$
Small	$\boldsymbol{V}_{\mathrm{S}1}(01001), \boldsymbol{V}_{\mathrm{S}2}(11010), \boldsymbol{V}_{\mathrm{S}3}(10100), \boldsymbol{V}_{\mathrm{S}4}(01101), \boldsymbol{V}_{\mathrm{S}5}(01010), \boldsymbol{V}_{\mathrm{S}6}(10110), \boldsymbol{V}_{\mathrm{S}7}(00101), \boldsymbol{V}_{\mathrm{S}8}(01011), \boldsymbol{V}_{\mathrm{S}9}(10010), \boldsymbol{V}_{\mathrm{S}10}(10101)$
Zero	$\boldsymbol{V}_0(00000), \boldsymbol{V}_{31}(11111)$

zero vectors ($\boldsymbol{V}_0, \boldsymbol{V}_{31}$), small vectors ($\boldsymbol{V}_{\mathrm{S}1} - \boldsymbol{V}_{\mathrm{S}10}$), medium vectors ($\boldsymbol{V}_{\mathrm{M}1} - \boldsymbol{V}_{\mathrm{M}10}$), and large vectors ($\boldsymbol{V}_{\mathrm{L}1} - \boldsymbol{V}_{\mathrm{L}10}$), as shown in Fig. 2(a). The space plane pattern is divided as ten sectors. The space angle range in each sector is $\pi/5$. Amplitudes of these large vectors, medium vectors, and small vectors can be expressed as

$$\begin{cases} V_{\mathrm{Large}} = V_{\max} = 2 * 2/5 * V_{\mathrm{dc}} * \cos 36^\circ = 0.6472\ \mathrm{V_{dc}} \\ V_{\mathrm{Middle}} = V_{mid} = 2/5 * \mathrm{V_{dc}} = 0.4\ \mathrm{V_{dc}} \\ V_{\mathrm{Small}} = V_{\min} = 2 * 2/5 * \mathrm{V_{dc}} * \cos 72^\circ = 0.2472\ \mathrm{V_{dc}} \end{cases} . \tag{3}$$

Thus, the active voltage vectors in the α-β subspace can be divided into three decagons, from inner decagon to outer decagon: D_1, D_2, D_3 [see Fig. 2(a)]. The ratio between two consecutive magnitudes is a constant of 0.618^{-1}. From Fig. 2, please note that the inner decagon D_1 in the α-β subspace is mapped as the outer decagon in the x-y subspace. The outer decagon D_3 in the α-β subspace is mapped as the inner decagon in the x-y subspace, but the middle decagon D_2 of the α-β subspace is still mapped as the middle decagon in the x-y subspace. The corresponding switching state of each voltage vector is summarized and listed in Table I.

B. Prediction Model of R–L Load

The load current dynamics can be described by the vector equation

$$\boldsymbol{V} = R\boldsymbol{i} + L\frac{d\boldsymbol{i}}{dt} \tag{4}$$

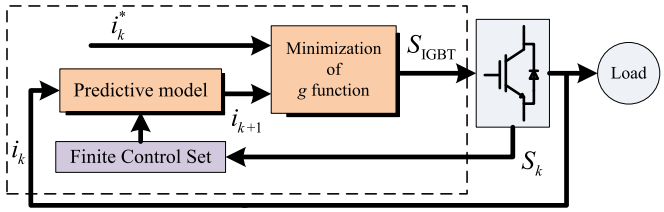

Fig. 3. Block diagram of traditional MPCC schemes.

where $\boldsymbol{V}$, $\boldsymbol{i}$ are the space voltage and current vectors in both α-β and x-y subspace. R, L represent the resistive and inductive loads. Assuming the small sampling interval T_{s}, and applying the first-order discrete approximation to voltage and current vector equations in (4), the future value of load current can be predicted as

$$\boldsymbol{i}(k+1) = \frac{1}{RT_{\mathrm{s}} + L}[L\boldsymbol{i}(k) + T_{\mathrm{s}}\boldsymbol{V}(k+1)] \tag{5}$$

where $\boldsymbol{V}(k+1)$ represents the candidate voltage vectors in the FCS. The term RT_{s} could be neglected if the sampling interval is small enough.

C. Traditional FCS-MPCC Schemes

The overall control diagram of the traditional FCS-MPCC for five-phase inverters is shown in Fig. 3. The predictive control scheme is performed in the following steps.

1) Measuring the load currents at kth sampling instant.
2) Predicting the load currents at $(k+1)$th sampling instant for all candidate voltage vectors in the FCS.
3) Evaluating the cost function value g for each prediction result.
4) Selecting the corresponding switching state that can minimize the cost function g from all candidate voltage vectors.

Once when the prediction and control time horizons are set, the cost function remains as the only tuning tool that exists in the FCS-MPCC. Typically, two forms of cost function are used, i.e., linear and quadratic [27]. For five-phase inverters, in order to achieve the sinusoidal current load waveform, not only the currents in α-β subspace need to be considered into the cost function, but also the harmonic currents in x-y subspace need to be contained. Therefore, the cost function must be relative to four current error terms, and usually defined as the following structures:

$$g = |i_\alpha^*(k+1) - i_\alpha(k+1)| + \left|i_\beta^*(k+1) - i_\beta(k+1)\right| + \lambda_1 |i_x^*(k+1) - i_x(k+1)| + \lambda_2 \left|i_y^*(k+1) - i_y(k+1)\right| \tag{6}$$

$$g = [i_\alpha^*(k+1) - i_\alpha(k+1)]^2 + [i_\beta^*(k+1) - i_\beta(k+1)]^2 + \lambda_1 [i_x^*(k+1) - i_x(k+1)]^2 + \lambda_2 [i_y^*(k+1) - i_y(k+1)]^2 \tag{7}$$

where i^* with the subscript represents the desired value of the corresponding currents in α-β and x-y subspace, respectively. λ_1 and λ_2 represent the weighting factors of cost function. In this

paper, the quadratic form is employed here as it can produce a higher penalization of bigger errors compared with smaller ones and better insight into the cost values. In addition, the differential process of cost function in (6) is very difficult, due to the expression type of the absolute value function. The expression of cost function in (7) is widely adopted in the FCS-MPCC schemes, especially in FCS-MPCC with duty-ratio optimization or pulse-width-modulation (PWM) stage [28]. Thus, quadratic form of cost function in (7) is also used in this paper.

In general, there are three classical FCS-MPCC schemes for a five-phase inverter according to the categories of the selected FCS. The FCS-MPCC that uses all the available switching states is termed as FCS-MPCC$_{31}$. All the ten largest voltage vectors and zero-voltage vectors are taken as the control set is named as the FCS-MPCC$_{11}$. Similarly, FCS-MPCC$_{21}$ method takes ten large vectors, ten medium vectors, and zero vectors as the input control set [27]. In essence, Lim *et al.* [27] have demonstrated that small vectors is not necessary to be included as elements in the input control set for the reason that small vectors in α-β subspace will become higher voltage vectors in the *x*-*y* harmonic subspace, which leads to large low-order current harmonics. In addition, the calculation burden of FCS-MPCC$_{21}$ and FCS-MPCC$_{31}$ schemes is very heavy.

Anyway, all of these traditional FCS-MPCCs applying a single switching state during each control interval, inevitably lead to an additional harmonic excitation in the *x*-*y* subspace, despite there are the harmonic component constraints in the predefined cost functions (6) and (7). In addition, in these three traditional FCS-MPCCs, the heavier computational efforts of the control scheme, the smaller low-order current harmonics. For example, computational burden in MPCC$_{31}$ is the heaviest, while the low-order current harmonic values are the smallest in these three schemes.

III. Proposed FCS-MPCC With Duty-Ratio Optimization

A. Definition of V^3s

As aforementioned, heavy computational burden and large low-order current harmonics are two existing key issues in the traditional FCS-MPCC of the five-phase drive system. According to (4), the harmonic currents $i_{\rm x}$, $i_{\rm y}$ are produced by the harmonic voltages existing in *x*-*y* subspace. Hence, if the harmonic average voltages are approximately zero in *x*-*y* subspace during each control interval, the harmonic currents $i_{\rm x}$, $i_{\rm y}$ can be eliminated effectively.

From Fig. 2(a) and (b), it can be noticed that the two inverter states with aligned large- and medium-voltage vectors in the α-β subspace, e.g., inverter states $\boldsymbol{V}_{\rm L1}$ and $\boldsymbol{V}_{\rm M1}$, become small- and medium-voltage vectors pointing to the opposite directions in the *x*-*y* subspace. On the basis of this principle, as the amplitude ratio between the medium- and small-voltage vectors is 0.618^{-1} in *x*-*y* subspace, the duration ratio of medium vector $\boldsymbol{V}_{\rm M1}$ and large vector $\boldsymbol{V}_{\rm L1}$ in α-β subspace can be set as 0.618 to synthesize a zero-mean volt–second product in the *x*-*y* subspace. The process is presented in Fig. 4. This combination mode of large and medium vectors and the corresponding dwell times design can eliminate low-order current distortion, and form ten active

Fig. 4. Schematic diagram of synthetic vectors $\boldsymbol{V}_{\rm v1}$ in different subspaces. (a) α-β subspace. (b) *x*-*y* subspace.

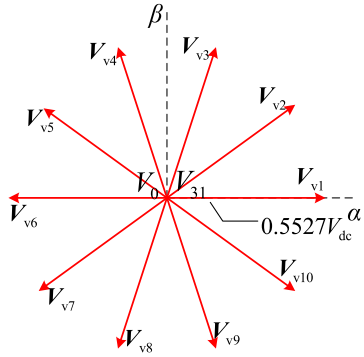

Fig. 5. V^3s in α-β subspace.

V^3s [29], named as $\boldsymbol{V}_{\rm v1} - V_{\rm V10}$, in α-β subspace, as shown in Fig. 5.

Following the above defined combination rule, the amplitudes of virtual vectors in α-β and *x*-*y* subspaces are expressed as

$$\begin{cases} |\boldsymbol{V}_v|_{\alpha\beta} = (1-k_v)\cdot 0.4\ \mathrm{V_{dc}} + k_v \cdot 0.6472\ \mathrm{V_{dc}} \\ |\boldsymbol{V}_v|_{\rm xy} = k_v \cdot 0.2472\ \mathrm{V_{dc}} - (1-k_v)\cdot 0.4\ \mathrm{V_{dc}} \end{cases} \tag{8}$$

where $k_{\rm v}$ represents duration ratio of the large-voltage vector during every control interval $T_{\rm s}$. Substituting $k_{\rm v} = 0.618$ into (8) yields

$$\begin{cases} |\boldsymbol{V}_v|_{\alpha\beta} = 0.5527\ \mathrm{V_{dc}} \\ |\boldsymbol{V}_v|_{\rm xy} = 0 \end{cases}. \tag{9}$$

Please note that the amplitudes of these 10 V^3s are all equal to $0.5527\,V_{\rm dc}$.

B. Cost Function Optimization

The goal of cost function is to adjust the system behavior through comparing the predicted values with reference values. It plays a great role in the FCS-MPCC scheme. For a five-phase drive system, in order to achieve sinusoidal current waveform and avoid current distortion in the *x*-*y* subspace, the harmonic current references i_x^* and i_y^* in cost function shown in (6) are both set to zero. In the proposed FCS-MPCC scheme, these 10 V^3s and zero-voltage vectors are set as the all available elements in the input control set. Thus, harmonic currents i_x and i_y can be eliminated automatically by the predefined V^3s. Therefore, the issue of low-order harmonic currents is unnecessary to be considered into cost function. In other words, the controlled quantities in the cost function are only current components in α-β subspace. The proposed FCS-MPCC scheme can reduce computational burden further. The modified cost function is

shown as

$$g = [i_\alpha^*(k+1) - i_\alpha(k+1)]^2 + [i_\beta^*(k+1) - i_\beta(k+1)]^2. \tag{10}$$

Please note that there is no weighting factor. It is easy to be implemented and applied in the practical application.

C. Digital Delay Compensation

As it is well known, in real-time implementation, one-step delay between the desired vector and the actual vector caused by digital processing will deteriorate the performance of FCS-MPCC, particularly when the calculation period is significant compared with the sampling period [30]. To compensate this delay, the digital delay compensation scheme in [30] is employed in this paper.

The measured currents and the applied switching state at the *k*th sampling instant are used in (5) to estimate the load current values at the $(k+1)$th sampling instant. Then, these estimated currents are used as the initial prediction values for all available vectors in the defined control set during $(k+2)$th control interval.

The prediction can be realized through one step forward shift of the load model, and cost function with the predicted currents during $(k+2)$th control interval is shown as

$$g = [i_\alpha^*(k+2) - i_\alpha(k+2)]^2 + [i_\beta^*(k+2) - i_\beta(k+2)]^2. \tag{11}$$

D. Duty-Ratio Determination

The optimization control object of MPCC is to force the predictive currents to reach the reference values. In traditional FCS-MPCC schemes, a single switching state is widely adopted during the entire control interval T_s, and it leads to large-current ripples, especially in the low-sampling-frequency condition. Although the V^3s are used as the input control set, they still cannot eliminate the tracking error completely. In most cases, it is not necessary for the V^3 being applied in the entire control interval to meet the desired control requirements. The corresponding duty ratio of the selected V^3 during each control interval should be estimated, in order to force the actual currents to track the reference values accurately. Thus, this paper proposes a combination solution of V^3 and zero-voltage vectors to further reduce tracking error. In this condition, if the dwell time of V^3 $\boldsymbol{V}_{\mathrm{v}j}$ during the entire control interval is defined as $d_j T_s$, zero-voltage vector is applied in the rest interval $(1-d_j)T_\mathrm{s}$, where d_j represents the duty ratio of virtual vector $\boldsymbol{V}_{\mathrm{V}j}$ during the entire control interval.

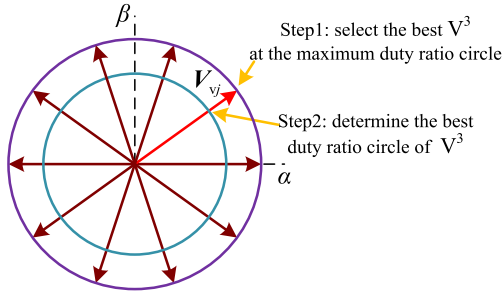

Fig. 6. Determination steps of d_j in the proposed FCS-MPCC scheme.

For the predictive current in α-β subspace, the computational expressions at $(k+2)$th sampling instant can be deduced from (4) as (12) shown at the bottom of this page. where $V_{\mathrm{v}j\alpha}$, $V_{\mathrm{v}j\beta}$ are α-axis and β-axis components of V^3 $\boldsymbol{V}_{\mathrm{V}j}$, respectively. The optimization control object is to minimize cost function g in (7) by selecting the appropriate duty ratio d_j, which yields

$$\frac{\partial g}{\partial d_j} = 0. \tag{13}$$

Substituting (11) and (12) into (13), d_j can be derived from (14). d_j is in the range from 0 to 1, and fortunately, the best solution d_j is irrelative to the weighting factor λ for the reason that harmonic currents are not contained into the adopted cost function, the computation process of d_j can be simplified (14) shown at the bottom of this page.

The first step of calculating d_j in the proposed method is to select an optimal V^3 or zero vector at the maximum duty-ratio value $(d_j = 1)$ from the cost function estimation for 11 times, and then, the best duty cycle of the selected V^3 can be deduced from (13), as shown in Fig. 6. The last step is to assemble pulse sequence units with V^3 and zero vector, which will be translated into the drive signals to five-phase inverters.

The first step of calculating d_j in the proposed method is to select an optimal V^3 or zero vector at the maximum duty-ratio value $(d_j = 1)$ from the cost function estimation for 11 times, and then, the best duty cycle of the selected V^3 can be deduced from (13), as shown in Fig. 6. The last step is to assemble pulse sequence units with V^3 and zero vector, which will be translated into the drive signals to five-phase inverters.

E. Switching Sequence and Implementation

Take $\boldsymbol{V}_{\mathrm{v}1}$ as an example, Fig. 7(a) shows the original combination switching sequence of the selected V^3 $\boldsymbol{V}_{\mathrm{v}1}$ and zero-

$$\begin{cases} i_\alpha(k+2) = \frac{1}{RT_\mathrm{s}+L}[Li_\alpha(k+1) + d_j T_\mathrm{s} V_{vj\alpha}(k+2)] \\ i_\beta(k+2) = \frac{1}{RT_\mathrm{s}+L}[Li_\beta(k+1) + d_j T_\mathrm{s} V_{vj\beta}(k+2)] \end{cases}, \quad j = 1, 2, ..., 10 \tag{12}$$

$$d_j = \frac{[V_{vj\alpha}(k+2)i_\alpha^* + V_{vj\beta}(k+2)i_\beta^*](RT_s + L) - L[V_{vj\alpha}(k+2)i_\alpha(k+1) + V_{vj\beta}(k+2)i_\beta(k+1)]}{T_\mathrm{s}[V_{vj\alpha}^2(k+2) + V_{vj\beta}^2(k+2)]}. \tag{14}$$

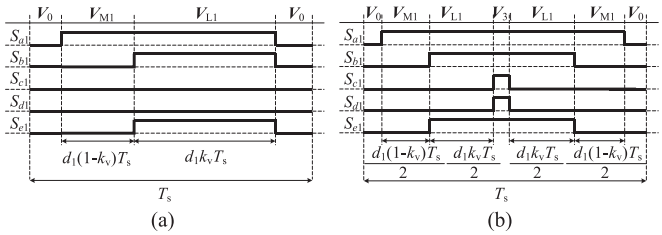

Fig. 7. Switching sequence of V^3 ($\boldsymbol{V}_{\mathrm{v1}}$). (a) Initial mode. (b) Symmetrical mode.

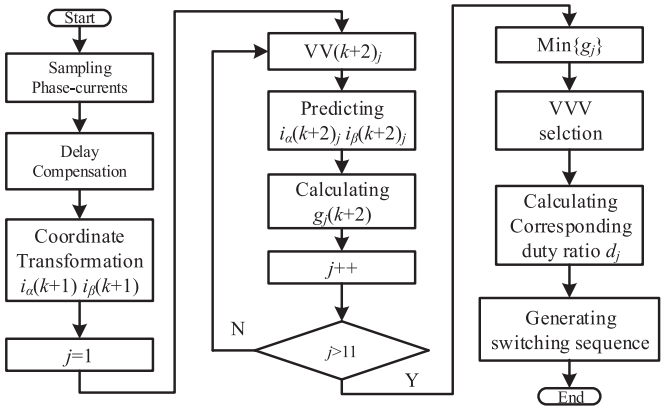

Fig. 8. Flowchart diagram of the proposed method.

voltage vectors, where the duration ratios of $\boldsymbol{V}_{\mathrm{M1}}$ and $\boldsymbol{V}_{\mathrm{L1}}$ are fixed at 0.618. Due to the asymmetry of this pulse sequence, there exists some additional harmonics around the switching frequency, and it is not easy to be realized in digital processors such as DSP TMS320F2000 series. For the most commonly used PWM generation technique, the inverted and noninverted signals are symmetrical to the middle of the PWM period. This type of PWM waves can be considered as the standard switching sequence for the real-time systems [26], [31]. Therefore, according to the specific PWM generation technique, symmetrical arrangement of switching sequence is first required, as presented in Fig. 7(b). Thus, the actual applied voltage vector sequences are changed from $\boldsymbol{V}_0 - \boldsymbol{V}_{\mathrm{M1}} - \boldsymbol{V}_{\mathrm{L1}} - \boldsymbol{V}_0$ to $\boldsymbol{V}_0 - \boldsymbol{V}_{\mathrm{M1}} - \boldsymbol{V}_{\mathrm{L1}} - \boldsymbol{V}_{31} - \boldsymbol{V}_{\mathrm{L1}} - \boldsymbol{V}_{\mathrm{M1}} - \boldsymbol{V}_0$. The corresponding duration of each switching state is shown in Fig. 7(b). The switching sequence in Fig. 7(b) is absolutely same with that of the traditional space vector PWM, which can realize constant switching frequency.

From the above analysis, the proposed FCS-MPCC scheme employing the V^{3}s as input control set is easy to be implemented. Moreover, the computational burden in the proposed FCS-MPCC is dramatically lower than that in the FCS-MPCC$_{21}$ method, because there are only 11 vectors for cost function evaluation during every control interval. Fig. 8 shows the flowchart diagram of the proposed V^3-FCS-MPCC$_{11}$ with duty-ratio optimization scheme. The block diagram for the proposed FCS-MPCC scheme is shown in Fig. 9, where the dashed box indicates the duty-ratio estimator. Compared to traditional FCS-MPCC, the simplicity structure is reserved.

IV. Simulation Results

To verify the effectiveness of the proposed FCS-MPCC with duty-ratio optimization scheme, a simulation comparison of the proposed scheme and four traditional FCS-MPCC schemes is shown in the MATLAB/Simulink environment. Five kinds of current control schemes are named as FCS-MPCC$_{11}$, FCS-MPCC$_{21}$, FCS-MPCC$_{31}$, FCS-MPCC$_{11-\mathrm{V}^3}$, and the proposed FCS-MPCC$_{11-\mathrm{V}^3-\mathrm{DRO}}$, respectively, where FCS-MPCC$_{11-\mathrm{V}^3}$ represents a form of traditional FCS-MPCC$_{11}$ scheme employing ten virtual vectors and zero vectors as the control set; FCS-MPCC$_{11-\mathrm{V}^3-\mathrm{DRO}}$ represents the proposed FCS-MPCC$_{11}$ with duty-ratio optimization of V^{3}s.

Fig. 10 shows steady-state simulation results of the output phase current, current fast Fourier transform (FFT) analysis, and current trajectories in two bidimensional subspaces for the traditional FCS-MPCC$_{11}$, FCS-MPCC$_{21}$, FCS-MPCC$_{31}$, FCS-MPCC$_{11-\mathrm{V}^3}$, and the proposed FCS-MPCC$_{11-\mathrm{V}^3-\mathrm{DRO}}$ scheme at same sampling frequency. In this figure, it is clear that the phase current waveform and the current ripples on two bidimensional subspaces in the proposed method are superior to the other four FCS-MPCC schemes. In addition, it should be noted that FCS-MPCC$_{21}$ and FCS-MPCC$_{31}$ methods can reduce the low-order current harmonics to a certain extent compared to the FCS-MPCC$_{11}$ scheme. Furthermore, Fig. 10(b) and (c) has verified that it is not necessary to set small vectors as elements in the control set.

Fig. 11 shows steady-state simulation results of the output phase current, current FFT analysis, and current trajectories in two bidimensional subspaces for five control schemes at same switching frequency. The average switching frequency in FCS-MPCC$_{31}$ and FCS-MPCC$_{11-\mathrm{V}^3}$ is about 5 kHz. Meanwhile, the switching frequency in the proposed FCS-MPCC$_{11-\mathrm{V}^3-\mathrm{DRO}}$ scheme is also set as 5 kHz. From Fig. 11, it is clear that the phase current waveform and the current ripples in the proposed FCS-MPCC$_{11-\mathrm{V}^3-\mathrm{DRO}}$ scheme under the same switching frequency is still superior to those in the adopted FCS-MPCC$_{31}$ and FCS-MPCC$_{11-\mathrm{V}^3}$, which has verified the effectiveness of the proposed scheme.

V. Experimental Results

Fig. 12 shows a scale-down experimental test setup of a five-phase inverter configuring with Infineon F4-30R06W1E3 insulated-gate bipolar transistor (30 A/600 V) modules. A dc power supply ($V_{\mathrm{dc}} = 40$ V) is fed for the adopted inverter with five-phase star-connected resistive–inductance loads ($R = 10\,\Omega$, $L = 4.5$ mH). The control scheme is programmed and implemented in TI DSP TMS320F28335. The output phase currents are measured with LA 35-NP current Hall sensors.

A. Steady-State Performance of Different FCS-MPCC Methods (Same Sampling Frequency)

In order to verify the feasibility of the proposed FCS-MPCC, at the same sampling frequency (10 kHz), Fig. 13 shows experimental results of current, phase voltage, current FFT analysis, and current trajectories in two bidimensional subspaces

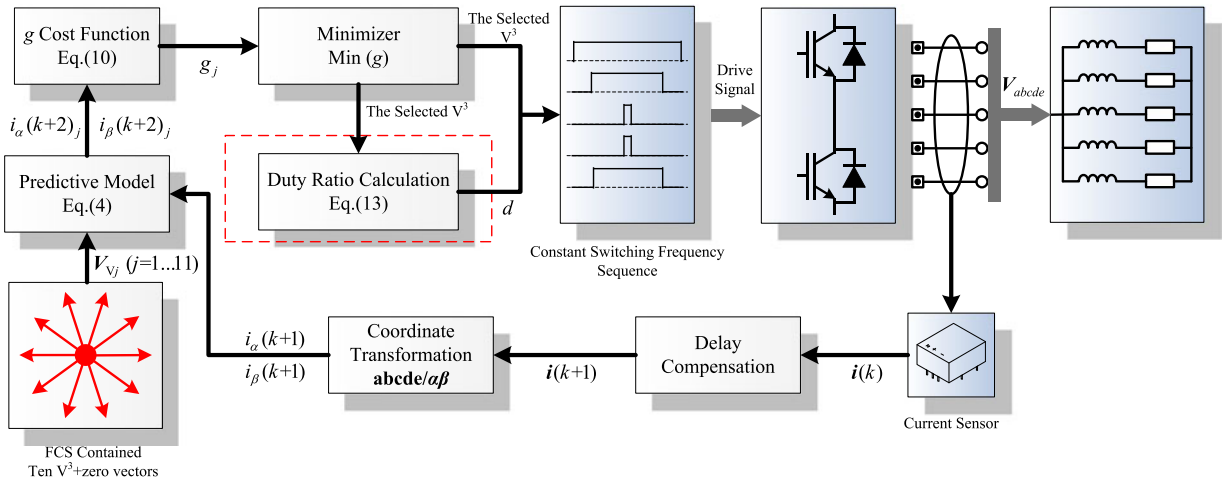

Fig. 9. Proposed FCS-MPCC$_{11-\mathrm{V}^3-\mathrm{DRO}}$ scheme of five-phase inverters.

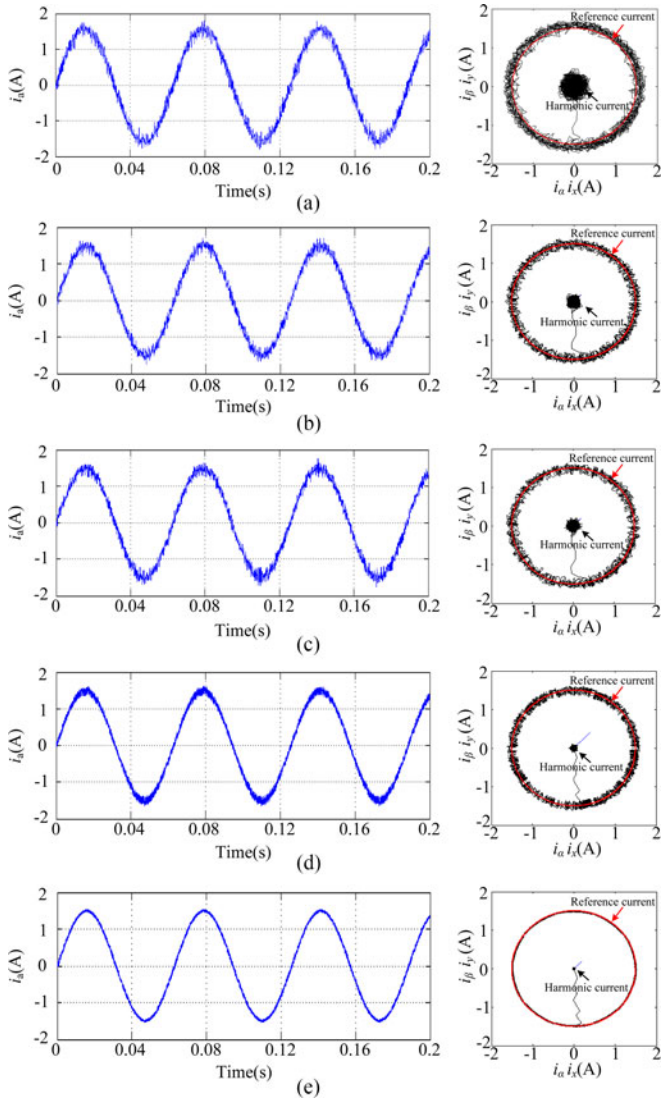

Fig. 10. Simulation comparison of steady-state performance for five FCS-MPCC schemes at same sampling frequency (10 kHz). (a) FCS-MPCC$_{11}$. (b) FCS-MPCC$_{21}$. (c) FCS-MPCC$_{31}$. (d) FCS-MPCC$_{11-\mathrm{V}^3}$. (e) Proposed FCS-MPCC$_{11-\mathrm{V}^3-\mathrm{DRO}}$ method.

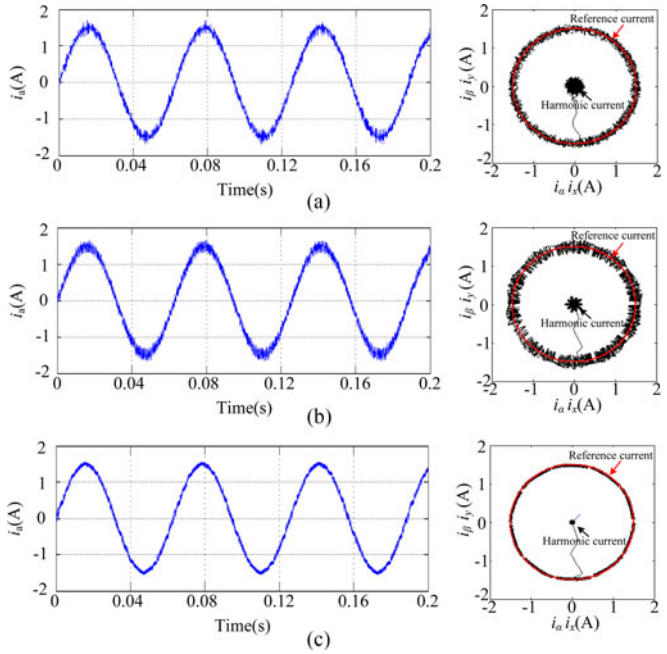

Fig. 11. Simulation comparison of steady-state performance for five FCS-MPCC schemes at same switching frequency (5 kHz). (a) FCS-MPCC$_{31}$. (b) FCS-MPCC$_{11-\mathrm{V}^3}$. (c) Proposed FCS-MPCC$_{11-\mathrm{V}^3-\mathrm{DRO}}$ method.

for the traditional FCS-MPCC$_{11}$, FCS-MPCC$_{11-\mathrm{V}^3}$, and the proposed FCS-MPCC$_{11-\mathrm{V}^3-\mathrm{DRO}}$ schemes. It is clear that the phase current waveform and the current ripples on two bidimensional subspaces in the proposed method are superior to the other two FCS-MPCC schemes. Current total harmonics distortion (THD_i) value in the proposed scheme is smallest $(\mathrm{THD}_i = 4.63\%)$. In Fig. 13(a), it can be found that although FCS-MPCC$_{11}$ scheme can suppress the harmonic currents in *x-y* subspace due to the cost function contained the harmonic items (7), there inevitably exists third- and seventh-order harmonic excitations in the *x-y* subspace because only a single switching vector is applied during each control interval. In Fig. 13(b), FCS-MPCC$_{11-\mathrm{V}^3}$ can reduce the harmonic currents in *x-y* sub-

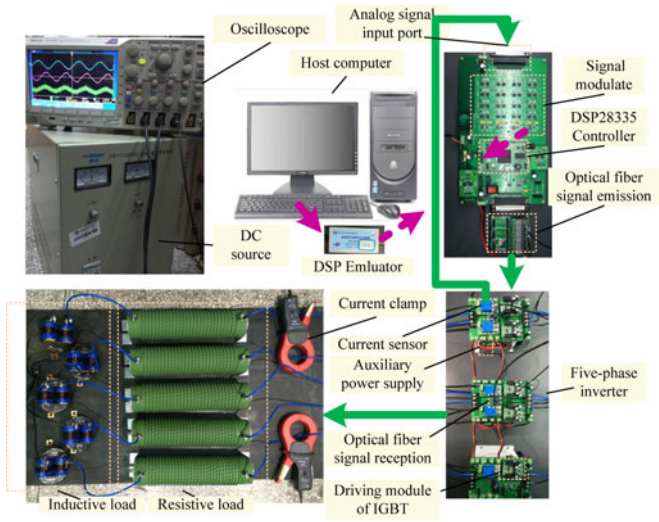

Fig. 12. Experimental configuration of a five-phase inverter test platform.

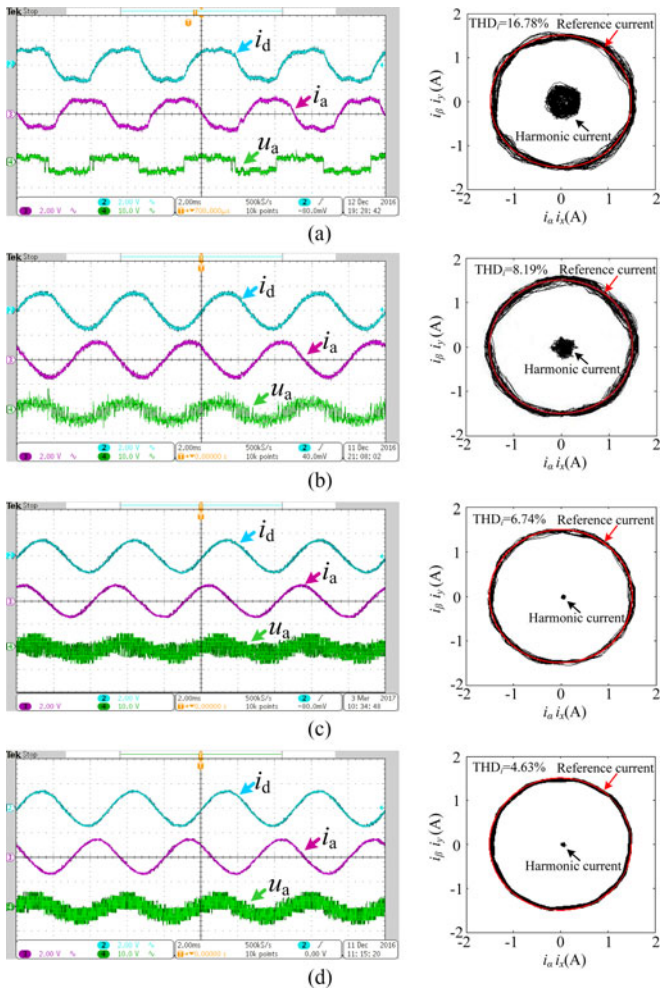

Fig. 13. Comparison of steady-state performance of various FCS-MPCC methods at same sampling frequency (10 kHz). (a) Traditional FCS-MPCC$_{11}$, (b) FCS-MPCC$_{11-\mathrm{V}^3}$, (c) proposed FCS-MPCC$_{11-\mathrm{V}^3-\mathrm{DRO}}$ method and proposed FCS-MPCC$_{11-\mathrm{V}^3-\mathrm{DRO}}$ with asymmetric switching sequence, and (d) proposed FCS-MPCC$_{11-\mathrm{V}^3-\mathrm{DRO}}$ method with symmetrical switching sequence.

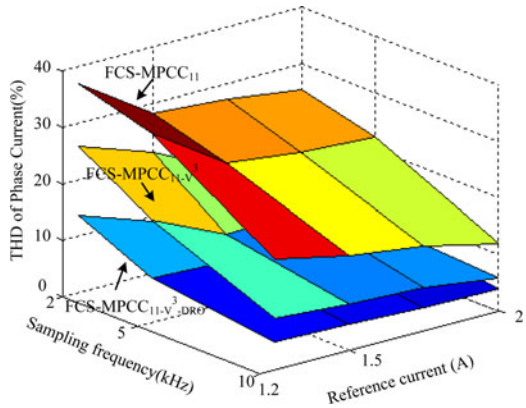

Fig. 14. Current THD values in three FCS-MPCCs with respect to different sampling frequency and reference current.

space partly. It should be mentioned that the average volt–second can be kept at zero when the instantaneous volt–second is still larger than that in the proposed FCS-MPCC$_{11-\mathrm{V}^3-\mathrm{DRO}}$ in each control interval, because FCS-MPCC$_{11-\mathrm{V}^3}$ is a special case of FCS-MPCC$_{11-\mathrm{V}^3-\mathrm{DRO}}$ with $d_j = 1$. Moreover, the current steady-state tracking error in α-β subspace cannot be eliminated completely. Fig. 13(c) and (d) shows experimental results of the proposed FCS-MPCC$_{11-\mathrm{V}^3-\mathrm{DRO}}$ scheme with asymmetric and symmetrical switching sequences, respectively. It is clear that the proposed FCS-MPCC$_{11-\mathrm{V}^3-\mathrm{DRO}}$ can further reduce more current ripples both in α-β and x-y subspaces compared with FCS-MPCC$_{11-\mathrm{V}^3}$ in Fig. 13(b). In addition, comparing Fig. 13(c) and (d), the symmetrical switching sequence scheme can achieve the better sinusoidal current quality and lower current THD$_i$ value than the asymmetric solution.

Fig. 14 shows current THD$_i$ values in three FCS-MPCCs with respect to different sampling frequency and reference current value. In this figure, it is clear that the proposed FCS-MPCC$_{11-\mathrm{V}^3-\mathrm{DRO}}$ can always achieve the smallest THD$_i$ value among the three FCS-MPCC schemes at different sampling frequency and reference current. The same sampling frequency means the same computing time for the execution of predictive control algorithm. For the traditional FCS-MPCC$_{11}$ and FCS-MPCC$_{11-\mathrm{V}^3}$, although the current quality can be improved in higher sampling frequency condition, the algorithm execution process period will be limited during shorter sampling interval. Fortunately, the proposed FCS-MPCC$_{11-\mathrm{V}^3-\mathrm{DRO}}$ can obtain better performance under the limitation of low sampling frequency, due to symmetrical switching sequence design with constant switching frequency.

B. Steady-State Performance of Different FCS-MPCC Methods (Same Switching Frequency)

To verify the effectiveness of the proposed scheme fairly, Fig. 15 shows a comparison of steady-state performance of FCS-MPCC$_{11-\mathrm{V}^3}$ and the proposed FCS-MPCC$_{11-\mathrm{V}^3-\mathrm{DRO}}$ methods at same switching frequency. The approximate switching frequency in FCS-MPCC$_{11-\mathrm{V}^3}$ is about 2.51 kHz when the

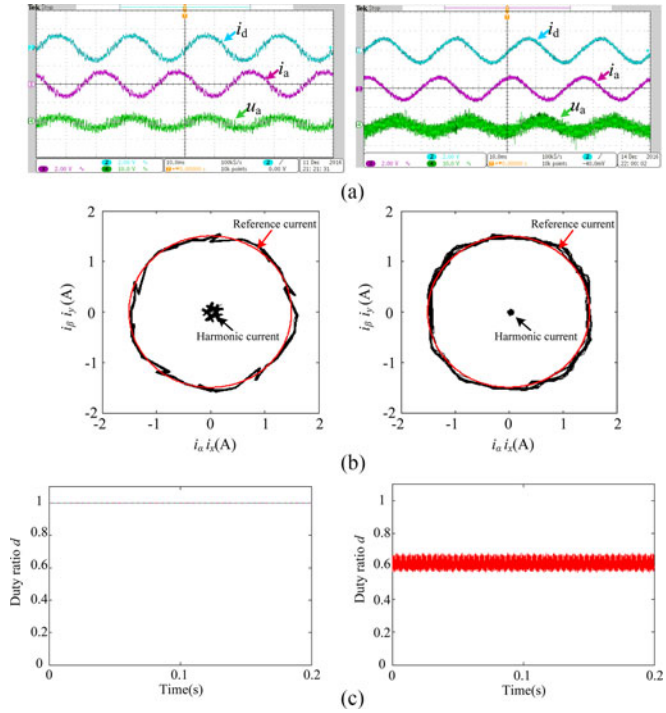

Fig. 15. Comparison of steady-state performance of two FCS-MPCC methods at same switching frequency (2 kHz). (a) Current waveform. (b) Current trajectories in *x*-*y* subspace. (c) Duty ratio.

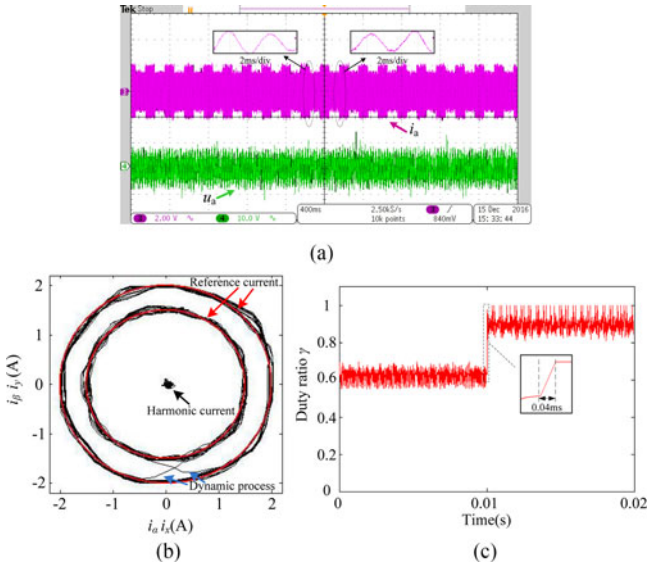

Fig. 16. Dynamic performances for a step in the reference current (2-kHz sampling frequency). (a) Current waveform. (b) Current trajectories. (c) Duty ratio.

sampling/control frequency is set to 5 kHz. Meanwhile, the switching frequency in the proposed FCS-MPCC$_{11-\mathrm{V}^3-\mathrm{DRO}}$ scheme keeps at 2 kHz even if the sampling/control frequency is set to 2 kHz. From Fig. 15, it is clear that the phase current waveform and the current ripples on two bidimensional subspaces of the proposed method under lower sampling and switching frequencies is still superior to those in the adopted FCS-MPCC$_{11-\mathrm{V}^3}$. Current THD$_i$ in the proposed scheme is 9.23% lower than 12.04% in FCS-MPCC$_{11-\mathrm{V}^3}$. In addition, the equivalent duty ratio of V^3 in the FCS-MPCC$_{11-\mathrm{V}^3}$ is always 1, while it is accurately estimated around 0.6 in the proposed method. The effectiveness of the proposed scheme is proved obviously from the other perspective.

C. Evaluation of Dynamic Performance for the Proposed FCS-MPCC$_{11-\mathrm{V}^3-\mathrm{DRO}}$ Method

As aforementioned, the proposed FCS-MPCC$_{11-\mathrm{V}^3-\mathrm{DRO}}$ method can both improve the steady-state current performance in α-β and *x*-*y* subspaces. In order to verify the dynamic performance of the current control in the proposed method, Fig. 16 shows the dynamic results for a step in the reference current at 2-kHz sampling frequency. It can be observed that the current in α-β subspace can always track the reference value precisely and achieve fast dynamic response. Meanwhile, from step change process of duty ratio, the current tracking ability for reference step change is very fast (settling time is approximately 0.04 ms). Moreover, the harmonic currents in *x*-*y* subspace are always kept at zero, thus sinusoidal phase current with low harmonic distortion is obtained.

D. Parameter Sensitivity Analysis of the Proposed FCS-MPCC$_{11-\mathrm{V}^3-\mathrm{DRO}}$ Method

The above experimental tests are carried on with the specific control parameters, i.e., $R = 10\ \Omega$, $L = 4.5$ mH. The load resistance has very small effect on the prediction process. In fact, it can be neglected for the reason that the sampling interval T_s is short enough. Therefore, the influence of inductance parameters variation on control performance should be mainly analyzed. First, the inductance mismatch ratio δ is defined as

$$\delta = 1 - \frac{L_m}{L} \tag{15}$$

where L_m is estimating inductance value and L is actual inductance value. L remains constant during the experiment.

Fig. 17 shows the steady-state performance of the proposed FCS-MPCC$_{11-\mathrm{V}^3-\mathrm{DRO}}$ method at 10-kHz sampling frequency, when the mismatch ratio δ is $+50\%$ and -50%, respectively, and the corresponding duty ratio is shown in Fig. 18. Compared with Fig. 13(d), it can be observed that there is no significant difference between these three sets of results. It confirms that the proposed FCS-MPCC$_{11-\mathrm{V}^3-\mathrm{DRO}}$ method is robust against the variation of control parameters. In order to clearly see the influence of inductance variation on the system, Fig. 19 shows the variation curve of phase current THD$_i$ and ripples in α-β and *x*-*y* subspaces with respect to inductance mismatch. It should be mentioned that the average steady-state ripples of currents in α-β and *x*-*y* subspaces in Fig. 13(d) are 0.0504 and 0.0483, respectively, which are very close to those in Fig. 17(a). However, the current ripples become slightly greater when the inductance mismatch ratio equals -20% and -50%.

Moreover, current THD$_i$ curve shown in Fig. 19 also presents the same trends. It can be noticed that from Fig. 19, the larger the absolute value of the inductance mismatch ratio δ is, the larger the current ripple and THD value are, and the negative ratio δ

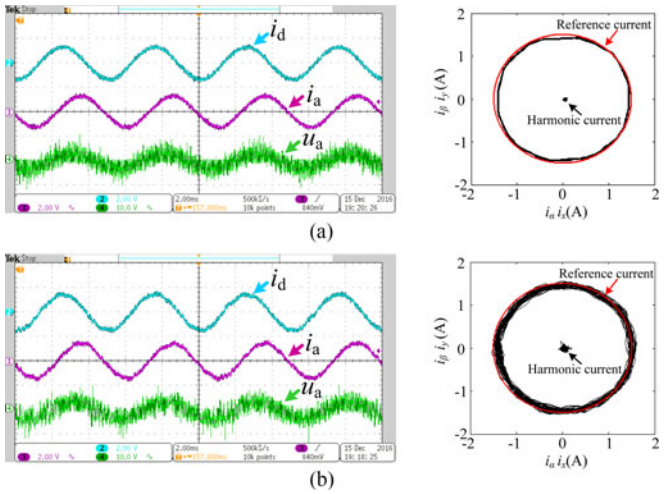

Fig. 17. Inductance mismatch effect on the load current. (a) $\delta = +50\%$. (b) $\delta = -50\%$.

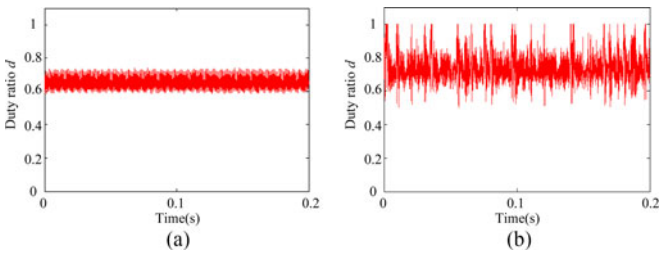

Fig. 18. Inductance mismatch effect on duty ratio. (a) $\delta = +50\%$. (b) $\delta = -50\%$.

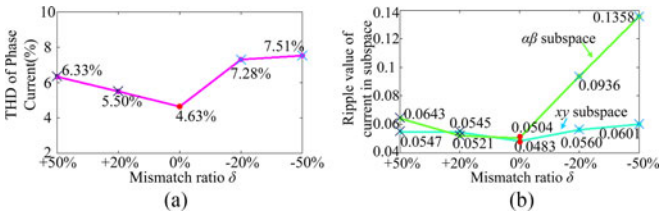

Fig. 19. (a) Variation curve of phase current THD. (b) Current ripples in α-β and x-y subspaces.

can result higher current ripple and THD values than the positive ratio δ in case of the same absolute value. Fortunately, current can still track the reference value in Fig. 17 no matter how the inductance changes. It has proved the strong robustness of the proposed FCS-MPCC scheme with duty-ratio optimization.

E. Cost Time Evaluation of the Proposed FCS-MPCC$_{11-\mathrm{V}^3-\mathrm{DRO}}$ Method

Fig. 20 shows the real-time implementation details of the proposed FCS-MPCC$_{11-\mathrm{V}^3-\mathrm{DRO}}$ scheme. It can be seen that the proposed FCS-MPCC$_{11-\mathrm{V}^3-\mathrm{DRO}}$ needs a sampling time of at least 40 μs. It means that the proposed scheme can still be executed below 20-kHz sampling frequency. The main time consuming is to iterate the predictive model and calculate the minimum cost function value while the duty-ratio calculation only occupies a tiny part during the entire execution period of the proposed scheme.

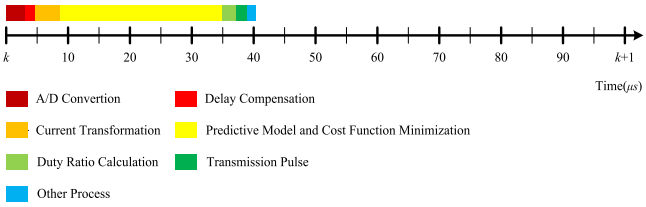

Fig. 20. Real-time implementation details of the proposed scheme in a sampling period.

TABLE II
EXPERIMENTAL COMPARISON OF THE PROPOSED CONTROL SCHEME AND OTHER SCHEMES

Control Schemes / Performances	FCS-MPCC$_{11}$	FCS-MPCC$_{21}$	FCS-MPCC$_{11-\mathrm{V}^3}$	FCS-MPCC$_{11-\mathrm{V}^3-\mathrm{DRO}}$
Steady-state current	General	Good	Good	Excellent
Dynamic performance	Fast	Fast	Fast	Fast
Cost effort	Easy	Heavy	Easy	Easy
The maximum available output voltage	0.6472 V_{dc}	0.6472 V_{dc}	0.5527 V	0.5527 V_{dc}

F. Comprehensive Comparison Performance of Three FCS-MPCC Schemes

Finally, a comprehensive comparison of the proposed FCS-MPCC scheme and two other methods is summarized and listed in Table II. The proposed scheme can achieve the best steady-state performance, and retain the fast transient performance as a potential feature in a traditional FCS-MPCC scheme. The proposed FCS-MPCC method is robust against the parameter mismatch. In addition, the computational consuming time for a whole control interval in the proposed FCS-MPCC is about 40 μs. Only ten V^{3}s and zero vectors need to be evaluated in every control interval. Moreover, it should be mentioned that the maximum available ac voltage of the proposed scheme is $0.5527\,V_{\mathrm{dc}}$ as shown in (9), which is smaller than that of the conventional FCS-MPCC scheme.

VI. CONCLUSION

This paper proposes an integrated FCS-MPCC method using V^{3}s as control set with duty-ratio optimization for five-phase inverters. In order to reduce the harmonic current and the calculation amount in the predictive control algorithm, ten V^{3}s are redefined in combination form of large- and medium-voltage vectors in the same direction in α-β subspace with constant duration ratio 0.618^{-1}. Thus, cost function can be simplified without weighting factor in the proposed FCS-MPCC. Actually, if the cost function does not contain the x-y current items, the controller could be less effective in dealing with nonideal effect, mainly caused by the dead-time effect. However, the effect is not quite significant. Therefore, in practical applications,

the *x-y* current items can be added into cost function depends on the property of the controller.

From a comprehensive experimental comparison of traditional FCS-MPCC, FCS-MPCC$_{11-\mathrm{V}^3}$, and the proposed FCS-MPCC$_{11-\mathrm{V}^3-\mathrm{DRO}}$ methods, the salient features of the proposed FCS-MPCC can be summarized as follows.

1) The steady-state phase current waveform and the current ripples on two bidimensional subspaces of proposed method are superior to the other FCS-MPCC schemes.
2) The proposed scheme can realize constant switching frequency.
3) The proposed scheme can retain the simplified structure and fast dynamic performance of traditional FSC-MPCC, which is easy to implement.
4) The proposed FCS-MPCC method is robust against the inductance mismatch.
5) The computational burden in the proposed FCS-MPCC is about 40 μs. The algorithm can be still executed under 20-kHz sampling frequency.
6) The proposed method takes the discrete feature of inverter into account with no modulation stage, avoided the complex computational process of desired voltage in generalized predictive control with PWM stage at the same time.

In this paper, a five-phase inverter is used as a practical example. Moreover, the proposed algorithm with duty-ratio optimization can be extended into *n*-phase inverter application.

REFERENCES

[1] E. Levi, "Multiphase electric machines for variable-speed applications," *IEEE Trans. Ind. Electron.*, vol. 55, no. 5, pp. 1893–1909, May 2008.

[2] E. Levi, "Advances in converter control and innovative exploitation of additional degrees of freedom for multiphase machines," *IEEE Trans. Ind. Electron.*, vol. 63, no. 1, pp. 433–448, Jan. 2016.

[3] F. Barrero and M. J. Duran, "Recent advances in the design, modeling, and control of multiphase machines—Part I," *IEEE Trans. Ind. Electron.*, vol. 63, no. 1, pp. 449–458, Jan. 2016.

[4] E. Jung, H. Yoo, S. K. Sul, H. S. Choi, and Y. Y. Choi, "A nine-phase permanent-magnet motor drive system for an ultrahigh-speed elevator," *IEEE Trans. Ind. Appl.*, vol. 48, no. 3, pp. 987–995, May/Jun. 2012.

[5] M. Darijevic, M. Jones, and E. Levi, "An open-end winding four-level five-phase drive," *IEEE Trans. Ind. Electron.*, vol. 63, no. 1, pp. 538–549, Jan. 2016.

[6] I. Gonzalez-Prieto, M. J. Duran, H. S. Che, E. Levi, M. Bermúdez, and F. Barrero, "Fault-tolerant operation of six-phase energy conversion systems with parallel machine-side converters," *IEEE Trans. Power Electron.*, vol. 31, no. 4, pp. 3068–3079, Apr. 2016.

[7] L. de Lillo *et al.*, "Multiphase power converter drive for fault-tolerant machine development in aerospace applications," *IEEE Trans. Ind. Electron.*, vol. 57, no. 2, pp. 575–583, Feb. 2010.

[8] N. K. Nguyen, F. Meinguet, E. Semail, and X. Kestelyn, "Fault-tolerant operation of an open-end winding five-phase PMSM drive with short-circuit inverter fault," *IEEE Trans. Ind. Electron.*, vol. 63, no. 1, pp. 595–605, Jan. 2016.

[9] S. Williamson and S. Smith, "Pulsating torque and losses in multiphase induction machines," *IEEE Trans. Ind. Appl.*, vol. 39, no. 4, pp. 986–993, Jul./Aug. 2003.

[10] L. Parsa, H. A. Toliyat, and A. Goodarzi, "Five-phase interior permanent-magnet motors with low torque pulsation," *IEEE Trans. Ind. Appl.*, vol. 43, no. 1, pp. 40–46, Jan./Feb. 2007.

[11] H. A. Toliyat, T. A. Lipo, and J. C. White, "Analysis of a concentrated winding induction machine for adjustable speed drive applications. II. Motor design and performance," *IEEE Trans. Energy Convers.*, vol. 6, no. 4, pp. 684–692, Dec. 1991.

[12] R. O. C. Lyra and T. A. Lipo, "Torque density improvement in a six-phase induction motor with third harmonic current injection," *IEEE Trans. Ind. Appl.*, vol. 38, no. 5, pp. 1351–1360, Sep./Oct. 2002.

[13] S. Kouro, P. Cortes, R. Vargas, U. Ammann, and J. Rodriguez, "Model predictive control—A simple and powerful method to control power converters," *IEEE Trans. Ind. Electron.*, vol. 56, no. 6, pp. 1826–1838, Jun. 2009.

[14] J. Rodriguez *et al.*, "Predictive current control of a voltage source inverter," *IEEE Trans. Ind. Electron.*, vol. 54, no. 1, pp. 495–503, Feb. 2007.

[15] A. Iqbal, H. Abu-Rub, P. Cortes, and J. Rodriguez, "Finite control set model predictive current control of a five-phase voltage source inverter," in *Proc. IEEE Int. Conf. Ind. Technol.*, Viña del Mar, Chile, 2010, pp. 1787–1792.

[16] P. Cortés, L. Vattuone, J. Rodriguez, and M. Duran, "A method of predictive current control with reduced number of calculations for five-phase voltage source inverters," in *Proc. Annu. Conf. IEEE Ind. Electron.*, Porto, Portugal, 2009, pp. 53–58.

[17] W. Xie *et al.*, "Finite-control-set model predictive torque control with a deadbeat solution for PMSM drives," *IEEE Trans. Ind. Electron.*, vol. 62, no. 9, pp. 5402–5410, Sep. 2015.

[18] C. S. Lim, N. A. Rahim, W. P. Hew, M. Jones, and E. Levi, "Model predictive current control of a five-phase induction motor," in *Proc. IEEE Annu. Conf. IEEE Ind. Electron.*, Melbourne, Vic., Australia, 2011, pp. 1934–1940.

[19] C. S. Lim, E. Levi, M. Jones, N. Abdul Rahim, and W. P. Hew, "Experimental evaluation of model predictive current control of a five-phase induction motor using all switching states," in *Proc. Int. Conf. Power Electron. Motion Contr.*, Novi Sad, Serbia, 2012, pp. LS1c.4-1–LS1c.4-7.

[20] P. Cortes, A. Wilson, S. Kouro, J. Rodriguez, and H. Abu-Rub, "Model predictive control of multilevel cascaded H-bridge inverters," *IEEE Trans. Ind. Electron.*, vol. 57, no. 8, pp. 2691–2699, Aug. 2010.

[21] C. S. Lim, N. A. Rahim, W. P. Hew, and E. Levi, "Model predictive control of a two-motor drive with five-leg-inverter supply," *IEEE Trans. Ind. Electron.*, vol. 60, no. 1, pp. 54–65, Jan. 2013.

[22] M. J. Duran, J. Prieto, F. Barrero, and S. Toral, "Predictive current control of dual three-phase drives using restrained search techniques," *IEEE Trans. Ind. Electron.*, vol. 58, no. 8, pp. 3253–3263, Aug. 2011.

[23] Y. Zhang and H. Yang, "Model predictive torque control of induction motor drives with optimal duty cycle control," *IEEE Trans. Power Electron.*, vol. 29, no. 12, pp. 6593–6603, Dec. 2014.

[24] S. A. Davari, D. A. Khaburi, and R. Kennel, "An improved FCS–MPC algorithm for an induction motor with an imposed optimized weighting factor," *IEEE Trans. Power Electron.*, vol. 27, no. 3, pp. 1540–1551, Mar. 2012.

[25] C. S. Lim, E. Levi, M. Jones, N. A. Rahim, and W. P. Hew, "A comparative study of synchronous current control schemes based on FCS-MPC and PI-PWM for a two-motor three-phase drive," *IEEE Trans. Ind. Electron.*, vol. 61, no. 8, pp. 3867–3878, Aug. 2014.

[26] H.-M. Ryu, J.-H. Kim, and S.-K. Sul, "Analysis of multiphase space vector pulse-width modulation based on multiple d-q spaces concept," *IEEE Trans. Power Electron.*, vol. 20, no. 6, pp. 1364–1371, Nov. 2005.

[27] C. S. Lim, E. Levi, M. Jones, N. A. Rahim, and W. P. Hew, "FCS-MPC-based current control of a five-phase induction motor and its comparison with PI-PWM control," *IEEE Trans. Ind. Electron.*, vol. 61, no. 1, pp. 149–163, Jan. 2014.

[28] W. Song, Z. Deng, S. Wang, and X. Feng, "A simple model predictive power control strategy for single-phase PWM converters with modulation function optimization, " *IEEE Trans. Power Electron.*, vol. 31, no. 7, pp. 5279–5289, Jul. 2016.

[29] L. Zheng, J. E. Fletcher, B. W. Williams, and X. He, "A novel direct torque control scheme for a sensorless five-phase induction motor drive," *IEEE Trans. Ind. Electron.*, vol. 58, no. 2, pp. 503–513, Feb. 2011.

[30] P. Cortes, J. Rodriguez, C. Silva, and A. Flores, "Delay compensation in model predictive current control of a three-phase inverter," *IEEE Trans. Ind. Electron.*, vol. 59, no. 2, pp. 1323–1325, Feb. 2012.

[31] Y. Ren and Z. Q. Zhu, "Reduction of both harmonic current and torque ripple for dual three-phase permanent-magnet synchronous machine using modified switching-table-based direct torque control," *IEEE Trans. Ind. Electron.*, vol. 62, no. 11, pp. 6671–6683, Nov. 2015.

Cheng Xue was born in Bengbu, Anhui, China, in 1994. He received the B.S. degree in electrical engineering from Southwest Jiaotong University, Chengdu, China, in 2015, where he is currently working toward the M.S degree in electrical engineering.

His current research interests include multiphase machine control and predictive control.

Wensheng Song (M'13) received the B.S. degree in electronic and information engineering and the Ph.D. degree in electrical engineering from Southwest Jiaotong University, Chengdu, China, in 2006 and 2011, respectively.

From September 2009 to September 2010, he was a Visiting Scholar with the Department of Electrical Engineering and Computer Science, University of California, Irvine, USA. From July 2015 to December 2015, he was a Visiting Scholar with the University of Alberta, Edmonton, Canada. He is currently an Associate Professor with the School of Electrical Engineering, Southwest Jiaotong University. His current research interests include digital control and modulation methods of electrical ac–dc–ac railway traction drive systems, and multilevel converters.

Xuesong Wu was born in Bengbu, Anhui, China, in 1994. He received the B.S. degree in electrical engineering from Southwest Jiaotong University, Chengdu, China, in 2016, where he is currently working toward the M.S. degree in electrical engineering.

His current research interests include power electronics and motor drives.

Xiaoyun Feng received the B.S., M.S., and Ph.D. degrees in electrical engineering from Southwest Jiaotong University, Chengdu, China, in 1983, 1988, and 2001, respectively.

She was a Visiting Professor with the University of Tokyo between October 1998 and October 1999. Since 1983, she has been with the School of Electrical Engineering, Southwest Jiaotong University, where she is currently a Full Professor. She is the author or coauthor of more than 70 papers. Her major research interests include the analysis and control of electrical traction converter and motor drive system, the design of railway traction characteristics, and train optimizing operation.